

B. Quackenbush¹, P. J. Atzberger^{1,2}

[1] Department of Mathematics, University of California Santa Barbara (UCSB).

[2] (corresponding author), Department of Mathematics, Department of Mechanical Engineering, University of California Santa Barbara (UCSB); atzberg@gmail.com; <http://atzberger.org/>

We introduce methods for obtaining pretrained Geometric Neural Operators (GNPs) that can serve as basal foundation models for use in obtaining geometric features. These can be used within data processing pipelines for machine learning tasks and numerical methods. We show how our GNPs can be trained to learn robust latent representations for the differential geometry of point-clouds to provide estimates of metric, curvature, and other shape-related features. We demonstrate how our pre-trained GNPs can be used (i) to estimate the geometric properties of surfaces of arbitrary shape and topologies with robustness in the presence of noise, (ii) to approximate solutions of geometric partial differential equations (PDEs) on manifolds, and (iii) to solve equations for shape deformations such as curvature driven flows. We also release a package of the codes and weights for using our pre-trained GNPs for processing point cloud representations. This allows for incorporating our pre-trained GNPs as components for reuse within existing and new data processing pipelines. The GNPs also can be used as part of numerical solvers involving geometry or as part of methods for performing inference and other geometric tasks.

Introduction

A recent development in machine learning has been to formulate and train models for reuse across a broad range of related tasks. These are often referred to as *foundation models* to indicate they are to be built upon similar to a foundation in order to perform further tasks [1, 2]. Prominent recent examples include large language models (LLMs) [3–5], image generation models [6–8], and object detection models [9–11]. Such approaches highlight the utility of having off-line training protocols and models with capabilities that are transferable to facilitate a wide range of tasks. Further specialized developments of shared off-line models even at smaller computational scales hold promise for impacting fields that include inference in scientific machine learning, physics-based feature extraction, and developing numerical solvers and simulations [12–15].

For geometric tasks, we introduce methods for developing pre-trained basal foundation models that are transferable for tasks involving geometry. Our approach allows for discovering geometric structures and geometric processing without the need for meshing and retraining to obtain information for down-stream tasks from general point-cloud representations. Our methods can be used to obtain estimates that include different types of curvatures, metrics, and other geometric features. Our methods also can be used as part of evaluation of differential operators on manifolds, exterior calculus operations, and other procedures that arise in geometric analysis and numerical solvers for geometric PDEs. Our training methods also incorporate approaches for obtaining estimates that are robust to noise or designed to deal with artifacts that can arise in point-cloud representation datasets. We show use cases for our pre-trained transferable GNP models, their robustness, and characterize other properties. These include (i) performing validation studies against test sets

involving topologies and geometric shapes not used in the training, (ii) computing deformations of shapes driven by mean-curvature flows, and (iii) developing geometric PDE solvers based on the GNP models. The results indicate the pre-trained GNPs can be used as data-driven alternatives to developing hand-crafted geometric estimators, which are often technical to formulate analytically and implement in practice. We release our codes and model weights in a package for use in training and for incorporating our pre-trained GNP models into other data processing pipelines and computational methods. The methods provide approaches for obtaining transferable GNP models for performing diverse geometric tasks.

We organize the paper as follows. We discuss how geometric features can be learned from point cloud representations using Geometric Neural Operators (GNPs) in Section 1. We discuss our approach to obtain transferable pre-trained GNPs for geometric tasks in Section 2. We discuss results for estimating metrics and curvatures, mean-flow shape changes, and development of numerical collocation solvers for geometric PDEs in Section 3.

1. Learning Geometric Features from Point Cloud Representations

Geometric contributions play an important role in many machine learning tasks, including features for shape classification, approximating deformations, or generation. Related contributions also play an important role in numerical tasks, including estimation of metrics or curvatures, and approximating solutions of PDEs on manifolds. Obtaining accurate and robust estimators for intrinsic geometric features and quantities can be difficult from discretely sampled data. Further, noise and other artifacts often arise in the data that presenting challenges. We develop data-driven methods for robustly obtaining geometric information from discretely sampled meshfree point cloud representations.

In our approach, we consider local regions of a manifold \mathcal{M} given in the form of a discrete set of points X and aim to learn a representation of the underlying geometry. In practice, a point $\mathbf{x} \in X$ is chosen to construct a neighborhood $\mathcal{N}_\epsilon(\mathbf{x})$ about \mathbf{x} , where $\epsilon = r_k\tau$, r_k is the radius of the k th nearest neighbor of \mathbf{x} , and τ is a user-specified parameter. Typically we set $\tau = 1.1$ and $k \in \{30, 50\}$. We center the data in the neighborhood about the mean $\bar{\mathbf{x}}$ and perform Principal Component Analysis (PCA) to obtain a local orthonormal basis such that each $\mathbf{y} \in \mathcal{N}_\epsilon(\mathbf{x})$ can be expressed as

$$\mathbf{y} = \bar{\mathbf{x}} + \xi^1(\mathbf{y})\boldsymbol{\psi}_1 + \xi^2(\mathbf{y})\boldsymbol{\psi}_2 + \xi^3(\mathbf{y})\boldsymbol{\psi}_3. \quad (1)$$

Provided the sampling of \mathcal{M} is sufficiently dense, we expect the vectors $\boldsymbol{\psi}_1, \boldsymbol{\psi}_2$ approximate well the tangent to the manifold at \mathbf{x} , and $\boldsymbol{\psi}_3$ approximates the normal to the manifold at \mathbf{x} . We set these vectors to be unit norm. To ensure the correct orientation, we assume that the orientation of the manifold on $\mathcal{N}_\epsilon(\mathbf{x})$ is known, and we set $\boldsymbol{\psi}_1 \times \boldsymbol{\psi}_2 = \boldsymbol{\psi}_3$ to be aligned with the outward normal at \mathbf{x} . One should note that $\boldsymbol{\psi}_1$ may no longer represent the principal direction of $\mathcal{N}_\epsilon(\mathbf{x})$.

The task can now be viewed as finding a Monge-Gauge parametrization of $\mathcal{N}_\epsilon(\mathbf{x})$,

$$\boldsymbol{\sigma}(\xi^1, \xi^2) = \bar{\mathbf{x}} + \xi^1\boldsymbol{\psi}_1 + \xi^2\boldsymbol{\psi}_2 + h(\xi^1, \xi^2)\boldsymbol{\psi}_3. \quad (2)$$

This amounts to finding a height function $h(\xi^1, \xi^2) = \xi^3$. Using this approach, all geometric quantities and differential operators can be computed using h and its derivatives. See Appendix A for details on computing relevant geometric quantities.

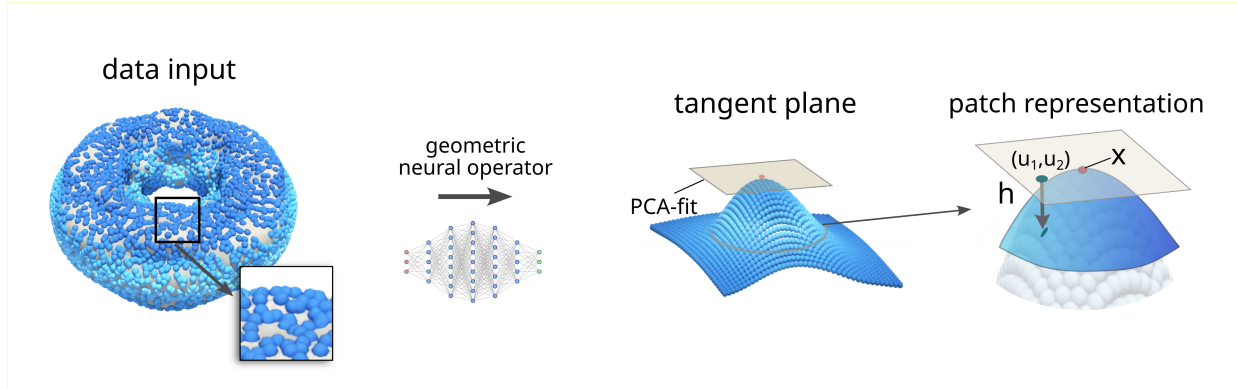


Figure 1: GNP for Geometric Representation Learning. We show how our GNP models use Geometric Neural Operators (GNPs) to capture latent geometric information from point-cloud representations.

We note that the change of coordinates to the basis $\{\psi_1, \psi_2, \psi_3\}$ ensure that any method for approximating the function h will be invariant to rotations and translations of the data, which do not affect the underlying geometry. We wish to additionally ensure that our model is robust to manifolds of varying scales, while maintaining the assumption of sufficient sampling density. While scale does impact geometric properties, any rescaling of the data can be done before model inference so that any data-derived model outputs are independent of the true scaling. For this reason, we consider a canonical rescaling of the coordinates to (u, v, w) , satisfying $(\epsilon u, \epsilon v, \delta w)$, where ϵ is the radius of the neighborhood. The parameter $\delta = \max(2\lambda, \delta_0)$, where λ is the standard deviation in the ψ_3 direction, and δ_0 is a user-specified parameter. This yields the Monge-Gauge parameterization to be

$$\sigma(u, v) = \bar{\mathbf{x}} + u\psi_1 + v\psi_2 + s(u, v)\psi_3, \quad (3)$$

where $u = \xi^1/c_1$, $v = \xi^2/c_2$, and $s(u, v) = h(\xi^1, \xi^2)/c_3$. The c_1, c_2, c_3 are characteristic scales that serve to standardize the representation of the local geometry. This plays a similar role to batch-normalization in other contexts of machine learning. We note that there are extreme cases where $\mathcal{N}_\epsilon(\mathbf{x})$ is (nearly) flat, in which case λ is nearly zero. In this case, $s(u, v)$ would likely fit noise arising from the data or, in the extreme case, round off error. To mitigate this issue, we introduce the user-specified parameter δ_0 and set it to 0.005 by default.

We choose to parameterize the function s in equation 3 using a basis $\Phi = \{\phi_1, \dots, \phi_N\}$. In particular, we consider a tensor product of 1D polynomials

$$\Phi = \{l_i(u)l_j(v)\}_{i,j=0}^N, \quad (4)$$

where l_i is the i th Legendre polynomial and $N = 3$. We note that this basis choice intentionally limits the expressivity of the approximation to s . For a sufficiently small neighborhood $\mathcal{N}_\epsilon(\mathbf{x})$, the shape should be well approximated by Φ and thus does not pose a problem. Further, the choice of a low-order polynomial basis ensures that the model is robust to noise and will not overfit to the data.

1.1. Geometric Neural Operators (GNPs)

We build on the neural operator framework [16, 17] to develop methods for learning patch representations from scattered data. In contrast to more conventional neural networks which map between

finite dimensional vector spaces, we use approaches that learn representations for operators that are not strictly tied to the underlying discretizations used for the input and output functions.

We use a geometric neural operator (GNP) [14] $\mathcal{G}_\theta : \mathcal{A} \rightarrow \mathcal{U}$, whose approximation consists of the following three learnable components (i) performing a lifting procedure \mathcal{P} for $a \in \mathbb{R}^{d_a}$ to a higher dimensional set of feature functions $v_0 \in \mathbb{R}^{d_v}$ with $d_v \geq d_a$, (ii) performing compositions of layers consisting of a local linear operator W , integral operator \mathcal{K} , bias function $b(\cdot)$, and non-linear activation $\sigma(\cdot)$, to obtain $v_{i+1} = \sigma(Wv_i + \mathcal{K}[v_i] + b)$, and (iii) performing projection \mathcal{Q} to a \mathbb{R}^{d_u} -valued function. The trainable components include the lifting procedure \mathcal{P} , kernel k , bias b function, and local operator W in the operator layers, and the projection \mathcal{Q} . We collect all of these parameters into θ . This gives a neural operator with T layers of the general form

$$\mathcal{G}_\theta^{(T)} = \mathcal{Q} \circ \sigma_T (W_T + \mathcal{K}_T + b_T) \circ \dots \circ \sigma_0 (W_0 + \mathcal{K}_0 + b_0) \circ \mathcal{P}. \quad (5)$$

The activation of the last layer σ_T is typically taken to be the identity. We consider linear operators \mathcal{K} of the form of the form

$$\mathcal{K}[v](x) = \int_D k(x, y)v(y) d\mu(y). \quad (6)$$

The μ is a measure on $D \subset \mathbb{R}^{d_v}$, $v : D \rightarrow \mathbb{R}^{d_v}$ is the input function, and k is a kernel $k(x, y) \in \mathbb{R}^{d_u} \times \mathbb{R}^{d_v}$. In practice, we compute this integral on a truncated domain $B_r(\mathbf{x})$ using message passing,

$$\tilde{\mathcal{K}}[v_t](\mathbf{x}_j) = \frac{1}{N} \sum_{x_k \in B_r(\mathbf{x}_j)} k(x_j, x_k)v_t(x_k). \quad (7)$$

For each layer t , we use a trainable kernel $k = k(x, y; \theta_t)$ parameterized by θ_t for fully connected neural networks having layer-widths (d_a, n, d_v^2) for $n \in \mathbb{N}$. We increase efficiency by using Nystrom approximation, summing over a subset of the points in $B_r(\mathbf{x}_j)$ instead of all points, using a maximum of 32 points in the sum. Further, we enforce a block-factorized structure in the outputs of the kernel network k as in [14]. In order to output a function representation, we apply average pooling to the outputs of \mathcal{G}_θ and pass this through two fully connected layers to obtain coefficients in the basis Φ as an approximation to the function $s(u, v)$ in equation 3. For more details also see [14].

2. Training GNPs to obtain Transferable Foundation Models for Geometric Tasks

We use radial manifolds with varying complexity to train the GNPs. Radial manifolds are surfaces that can be connected to the origin by a line segment that intersects the surface at only one point. Further, we developed a spectral method using spherical harmonics to generate the ground truth data for training with the aid of the sphericart Python package, see [18]. We generated 320 total manifolds with varying complexities for training, and 40 for testing. All data contained 100,000 points along with normal vectors at each point. Further, we recorded the first and second fundamental forms, as well as the Gaussian curvature to use in training.

For training, neighborhoods $\mathcal{N}_\epsilon(\mathbf{x})$ are chosen using a randomly selected center \mathbf{x} and querying all points within the ϵ -neighborhood for a user specified number of nearest neighbors k using a KD-tree. To ensure accurate approximation of the geometry near the boundary of $\mathcal{N}_\epsilon(\mathbf{x})$,

we include all points within radius 1.5ϵ of \mathbf{x} to be input to the model \mathcal{G}_θ , but only evaluate the output on the points within $\{(u_i, v_i, w_i)\}_{i=1}^N := \mathcal{N}_\epsilon(\mathbf{x})$. To ensure that \mathcal{G}_θ accurately captures the geometry of the neighborhood, we convert our ground truth data of the first two fundamental forms $\{\mathbf{I}\}_{i=1}^N, \{\mathbf{II}\}_{i=1}^N$ from the spherical frame they were computed in to the local frame given by $\{\boldsymbol{\psi}_1, \boldsymbol{\psi}_2, \boldsymbol{\psi}_3\}$. We choose to train on the matrix inverse of the first fundamental form \mathbf{I}_i^{-1} , to ensure that our model will approximate differential operators that use \mathbf{I}_i^{-1} and its derivatives. In addition, we use the outward normals $\{\boldsymbol{\eta}_i\}_{i=1}^N$ and the Gaussian curvature $\{K_i\}_{i=1}^N$ at each point (u_i, v_i, w_i) . We then can predictions for all of these quantities by constructing the function $\hat{s}(u, v)$ from the coefficients given by $\mathcal{G}_\theta(\mathcal{N}_\epsilon(\mathbf{x}))$. We then compute the loss for a single neighborhood as

$$\begin{aligned} \mathcal{L}(\mathcal{N}_\epsilon(\mathbf{x}); \theta) := & \mathcal{L}_{\text{rel}}(\{\hat{s}(u_i, v_i)\}, \{w_i\}) + \lambda_1 \mathcal{L}_\eta(\{\hat{\boldsymbol{\eta}}_i\}, \{\boldsymbol{\eta}_i\}) + \lambda_2 \mathcal{L}_{\text{rel}}\left(\{\hat{\mathbf{I}}_i^{-1}\}, \{\mathbf{I}_i^{-1}\}\right) \\ & + \lambda_3 \mathcal{L}_{\text{rel}}\left(\{\hat{\mathbf{II}}_i\}, \{\mathbf{II}_i\}\right) + \lambda_4 \mathcal{L}_{\text{rel}}\left(\{\hat{K}_i\}, \{K_i\}\right), \end{aligned} \quad (8)$$

where we define the relative loss as

$$\mathcal{L}_{\text{rel}}(f, g) = \frac{\|f - g\|_2}{\|f\|_2}, \quad (9)$$

and the normal loss as

$$\mathcal{L}_\eta(\{\hat{\boldsymbol{\eta}}_i\}, \{\boldsymbol{\eta}_i\}) = \frac{1}{N} \sum_{i=1}^N (1 - \hat{\boldsymbol{\eta}}_i \cdot \boldsymbol{\eta}_i). \quad (10)$$

We set $\lambda_n = 0.5$ for $n = 1, 2, 3, 4$. When training with a batch size greater than 1, we compute the mean of this loss over each of the neighborhoods. We use this training protocol in the noise-less case and when we apply a small amount of Gaussian noise to every point with standard deviation 10^{-3} . Additionally, we consider a case where we add Gaussian noise with a larger standard deviation of 5×10^{-3} to only 10 we do not evaluate the loss function on the noisy points so that the model learns to identify and ignore them.

3. Results

3.1. Validation Studies for Curvature and Other Geometric Quantities

We perform validation studies of the geometric quantities on two generated datasets. We consider one testing dataset of 40 radial manifolds that is similar to the training data, and another of 40 toroidal manifolds. For specifics on the generation of these two datasets, see Appendix B. We use two datasets for validation to show consistency in our models performance across different topologies. We test the performance of the model using the same losses as in equations 9 and 10. During training these losses are computed over the neighborhoods, but for validation we compute these losses over the entire point cloud of 100,000 points, and average across all 40 manifolds. We present the results in Table 1 and note consistency between the two datasets. Further, we note the accuracy in the mean curvature of the model, which was not present in the loss function. This demonstrates that the Weingarten map \mathbf{W} (see Appendix A) is being accurately approximated by the model when training with our loss function in equation 8.

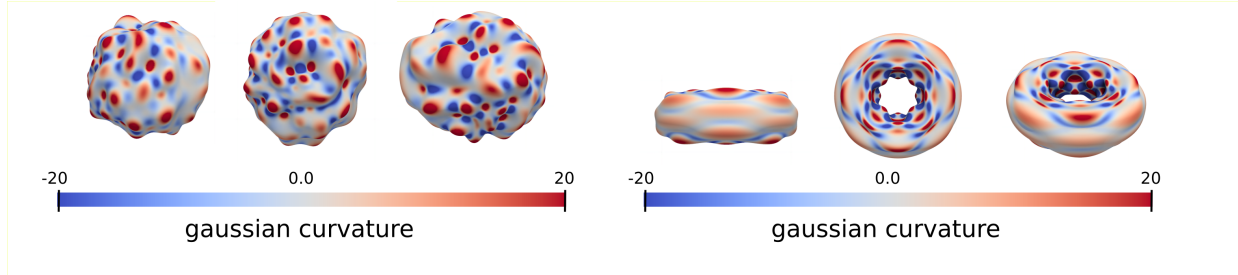


Figure 2: GNP Model Estimates of Gaussian Curvatures. We show results for a radial manifold (left) and a toroidal manifold (right) which differs.

model	k	normal	metric inverse	shape	gaussian	mean
radial manifolds						
clean	30	2.04e-06	6.57e-04	1.89e-02	4.07e-02	1.93e-02
clean	50	4.55e-06	7.99e-04	1.70e-02	4.56e-02	2.24e-02
outliers, $\sigma = 5e-03$,	50	3.70e-05	1.97e-03	2.75e-02	6.26e-02	3.14e-02
noise, $\sigma = 1e-03$,	70	6.10e-05	5.62e-03	1.32e-01	1.75e-01	1.03e-01
toroidal manifolds						
clean	30	6.19e-07	3.79e-05	2.30e-02	4.03e-02	2.50e-02
clean	50	1.43e-06	6.07e-05	2.48e-02	4.38e-02	3.34e-02
outliers, $\sigma = 5e-03$	50	4.16e-05	2.11e-04	3.71e-02	6.31e-02	4.45e-02
noise, $\sigma = 1e-03$	70	7.80e-05	6.25e-04	1.54e-01	2.16e-01	1.19e-01

Table 1: Accuracy and Robustness of the GNP Models. We show the accuracy and robustness of the GNP estimates for curvature for the radial and toroidal manifolds. We show how the accuracy of the models are impacted by the presence of noise or outlier artifacts. We also show how the number of neighbors k used to construct $\mathcal{N}_\epsilon(\mathbf{x})$ impacts the GNP model’s performance.

3.2. Shape Deformations Driven by Mean Curvature Flows

We demonstrate the use of the pre-trained GNPs for simulations of mean curvature flows on surfaces. Given an initial smooth surface \mathcal{M} and an initial immersion $\varphi_0 : \mathcal{M} \rightarrow \mathbb{R}^3$, the mean curvature flow (MCF) is a family of smooth immersions $\varphi_t : \mathcal{M} \rightarrow \mathbb{R}^3$ for $t \in [0, T)$ such that the function $\varphi(p, t) = \varphi_t(p)$ is a solution of the PDE:

$$\begin{cases} \frac{\partial}{\partial t} \varphi(p, t) = H(p, t) \boldsymbol{\eta}(p, t), & p \in \mathcal{M}, t \in [0, T), \\ \varphi(p, 0) = \varphi_0(p), & p \in \mathcal{M}, \end{cases} \quad (11)$$

where $H(p, t)$, $\boldsymbol{\eta}(p, t)$ denote the mean curvature and outward unit normal at $p \in \mathcal{M}$ at time t . Intuitively this flow moves the surface in the direction of the normal vector at a rate proportional to the mean curvature. We simulate the MCF on 4 different initial test shapes shown in Figure 3, the first 3 of which were obtained from [19] and [20]. At each time step t_n and each point \mathbf{x}_i^n , we advance the method by one time step using for each i :

$$\mathbf{x}_i^{n+1} = \mathbf{x}_i^n + \Delta t H(\mathbf{x}_i^n) \boldsymbol{\eta}(\mathbf{x}_i^n), \quad (12)$$

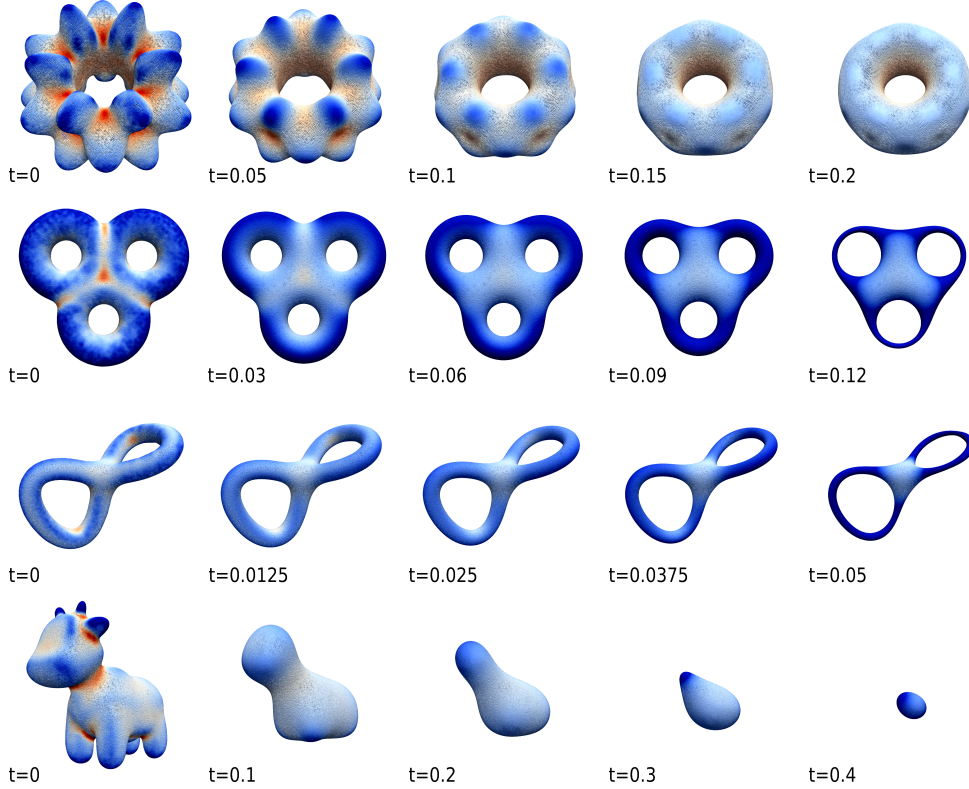


Figure 3: Shape Deformations from Curvature-Driven Flows based on GNPs. We show how shape deformations evolve under curvature-driven flows that use estimates from the GNP models.

where $H(\mathbf{x}_i^n)$, $\boldsymbol{\eta}(\mathbf{x}_i^n)$ are the mean curvature and normal vector at \mathbf{x}^n . We set $\Delta t = 10^{-4}$ and use our pretrained GNP to estimate $H, \boldsymbol{\eta}$ at \mathbf{x}_i^n for all i, n .

To ensure stability of the method, we apply a smoothing step on the values of H before marching in time using equation 12. Namely, we replace $H(\mathbf{x}_i^n)$ by $\tilde{H}(\mathbf{x}_i^n)$ defined as

$$\tilde{H}(\mathbf{x}_i^n) = C_i^n \sum_{\mathbf{x}_j^n \in B(\mathbf{x}_i^n, 3r_0)} w(\|\mathbf{x}_j^n - \mathbf{x}_i^n\|_2) H(\mathbf{x}_j^n), \quad w(r) = \exp(-r^2/(2r_0^2)) \quad (13)$$

where C_i^n is chosen so that the weights $w(\|\mathbf{x}_j^n - \mathbf{x}_i^n\|_2)$ sum to 1. In practice we set $r_0 = 0.00667$. Additionally, as time evolves, areas of negative mean curvature will shrink and point samplings will become more dense. In order to maintain quasi-uniformity of the points, we subsample in areas of high density, ensuring that we still get good coverage of the surface.

We run the simulation for 4000 time steps for each shape, and show the results in Figure 3. It is known that certain shapes will develop singularities in finite time, and we observe this behavior in the simulations. We show the results up until the first singularity occurs for the second and third shapes in Figure 3.

3.3. Using GNPs to Develop Numerical Methods for Geometric PDEs

We demonstrate the use of our transferable GNP models in collocation methods for solving geometric PDEs on surfaces. We use the pre-trained GNPs for estimation of the needed geometric quantities arising in the differential operators of the PDE. We develop solvers for the Laplace-Beltrami PDE

$$\begin{cases} \Delta_{LB} u & = -f, \\ \int_{\mathcal{M}} u(\mathbf{x}) d\mathbf{x} & = 0 \\ \Delta_{LB} & = \frac{1}{\sqrt{|g|}} \partial_i \left(g^{ij} \sqrt{|g|} \partial_j \right), \end{cases} \quad (14)$$

where g is the metric tensor and g^{ij} are components of the inverse metric tensor. For solving this PDE, we need to have reliable numerical estimators for the metric g and derivatives of the inverse metric tensor components g^{ij} . We show collocation methods can be developed by using our pre-trained GNPs to obtain the geometric contributions and Generalized Moving Least Squares (GMLS) approximations to interpolate the surface field $u(x)$. This differs from our prior work [21] where we used GMLS and analytic expressions to obtain both numerical estimators of the geometric quantities and the surface fields. A issue that can arise in GMLS methods is inaccuracies and instabilities in the approximations from the least-square fits in the presence of outliers, noise, and other types of artifacts in the point-cloud representations. A key aspect of the work we present here is the use of the transferable pre-trained GNP models to estimate the geometric contributions, allowing for data-driven approaches for that filter out artifacts in the point-cloud representations.

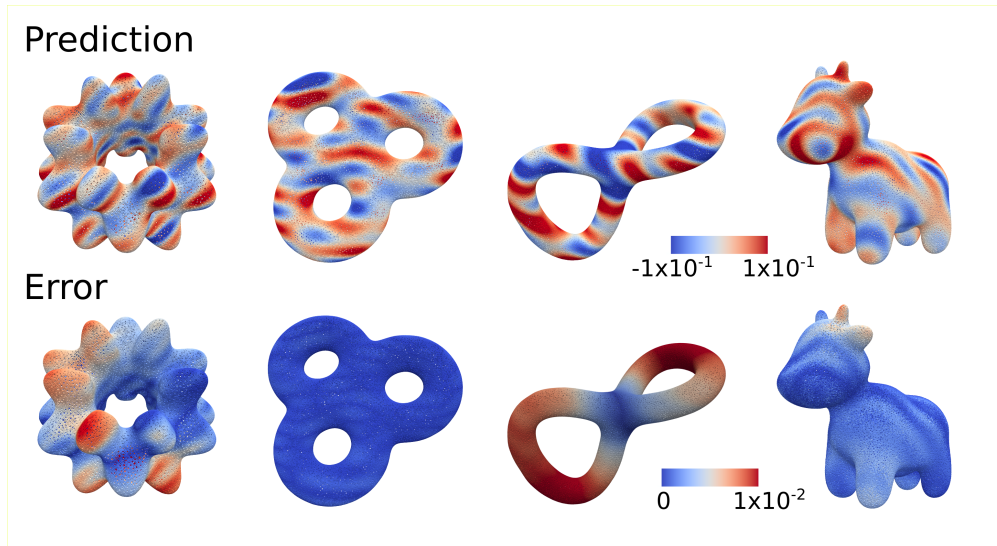


Figure 4: GNP Numerical Methods for Geometric PDEs. We show the results of the Laplace-Beltrami solver for a few shapes.

We consider the Laplace-Beltrami operator Δ_{LB} on a surface \mathcal{M} , and use GMLS with our pretrained GNP to approximate the action of Δ_{LB} on a function $u : \mathcal{M} \rightarrow \mathbb{R}$. At each point \mathbf{x} on the surface, we solve a local least squares problem on data $\mathbf{x}_{j=1}^n$ in a neighborhood $\mathcal{N}_\epsilon(\mathbf{x})$ to

model	k	bumpy torus	3 torus	2 torus	cow
clean	30	7.97e-02	9.55e-03	8.23e-02	7.11e-02
clean	50	8.49e-02	1.26e-02	3.86e-02	9.93e-02
outliers, $\sigma = 5e-03$	50	9.30e-02	1.72e-02	6.94e-02	1.08e-01
noise, $\sigma = 1e-03$	70	9.95e-02	2.02e-02	5.52e-02	1.02e-01

Table 2: Accuracy and Robustness of the GNP Numerical Methods for Geometric PDEs. Mean relative L^2 -error for the GNP numerical methods for geometric PDE.

approximate u and its derivatives at \mathbf{x} . Namely we consider the basis Φ in section 1 to solve for

$$p^* = \arg \min_{q \in \Phi} \sum_{j=1}^n (u(\mathbf{x}_j) - q(\mathbf{x}_j))^2 w(\|\mathbf{x}_j - \mathbf{x}\|_2), \quad (15)$$

where w is a compactly supported positive weight function. For a weight function w , we choose $w(r) = (1 - \frac{r}{\epsilon})_+^4$, where $(z)_+ = \max(z, 0)$. Once the best approximation p^* is found, we use the pre-trained GNP to compute the action of Δ_{LB} on p^* . This can be summarised as

$$\Delta_{LB} p^*(\mathbf{x}) = \Delta_{LB}(\mathbf{P})^T (\Lambda(\mathbf{P})^T \mathbf{W} \Lambda(\mathbf{P}))^{-1} \Lambda(\mathbf{P})^T \mathbf{W} \Lambda(u) \quad (16)$$

where $\Delta_{LB}(\mathbf{P}) \in \mathbb{R}^{\dim \Phi}$ is the matrix of the Laplace-Beltrami operator applied to the basis functions Φ at \mathbf{x} . The $\Lambda(\mathbf{P}) \in \mathbb{R}^{n \times \dim \Phi}$ denotes the matrix whose (i, j) -entry is $\phi_i(\mathbf{x}_j)$. The $W \in \mathbb{R}^{n \times n}$ denotes the diagonal matrix of weights $w(\|\mathbf{x}_j - \mathbf{x}\|_2)$. The $\Lambda(u) \in \mathbb{R}^n$ is the vector of function values $u(\mathbf{x}_j)$. We perform tests by using our numerical solver for the Laplace-Beltrami equation on the shapes shown in Figure 3. We generate functions u on \mathbb{R}^3 using random fourier modes up to a frequency of 10, and compute the action of Δ_{LB} on u using for training data GMLS geometric quantities. We then shift and rescale u and f , respectively, so that u satisfies the boundary condition and f takes values within $[-20, 20]$.

We use collocation to solve the Laplace-Beltrami equation. We solve $A\tilde{u} = \tilde{f}$ where \tilde{f} is the data vector of f at the points \mathbf{x}_j , and A is the stiffness matrix acquired from the GMLS interpolation for u in equation 15. To ensure that we have a consistent system, we use all 100,000 points of \tilde{f} but solve for 90,000 points of \tilde{u} . We minimize residuals by solving the system $A^T A \tilde{u} = A^T \tilde{f}$ using Scipy’s LGMRES solver and algebraic multigrid preconditioner using PyAMG [22]. Results are shown in Table 2.

Conclusions

We have shown how GNPs can be trained to obtain transferable models for use in diverse geometric tasks. Our approaches learn robust models by training on prescribed noisy datasets for filtering out artifacts. We demonstrate the approaches on a few example tasks. This includes the estimation of metrics and curvatures, deformations from shape-driven flows, and development of numerical solvers for geometric PDEs. We also release an open source package with training codes and with our weights for pre-trained GNPs. This allows for incorporating our GNP models into other data processing pipelines and computational methods. The approaches provide methods for obtaining transferable GNP models for performing diverse geometric tasks.

Open Source Package

We release an open source package for our methods at https://github.com/atzberg/geo_neural_op.

Acknowledgments

Authors research supported by grant NSF Grant DMS-2306101. Authors also would like to acknowledge computational resources and administrative support at the UCSB Center for Scientific Computing (CSC) with grants NSF-CNS-1725797, MRSEC: NSF-DMR-2308708, Pod-GPUs: OAC-1925717, and support from the California NanoSystems Institute (CNSI) at UCSB. P.J.A. also would like to acknowledge a hardware grant from Nvidia.

References

- [1] Rishi Bommasani et al. “On the opportunities and risks of foundation models”. In: *arXiv preprint arXiv:2108.07258* (2021).
- [2] Thomas M Breuel. “Reflections on Foundation Models”. In: *Stanford HAI* (2021). URL: <https://crfm.stanford.edu/2021/10/18/reflections.html>.
- [3] Hugo Touvron et al. “Llama: Open and efficient foundation language models”. In: *arXiv preprint arXiv:2302.13971* (2023).
- [4] Mikhail V Koroteev. “BERT: a review of applications in natural language processing and understanding”. In: *arXiv preprint arXiv:2103.11943* (2021).
- [5] OpenAI. *ChatGPT*. [Large language model]. 2023. URL: <https://chat.openai.com/chat>.
- [6] OpenAI. *DALL-E-3*. [Image Generation Model]. 2024. URL: <https://openai.com/index/dall-e-3/>.
- [7] Dustin Podell et al. “Sdxl: Improving latent diffusion models for high-resolution image synthesis”. In: *arXiv preprint arXiv:2307.01952* (2023).
- [8] Midjourney. *Midjourney*. [Image Generation Model]. 2024. URL: <https://www.midjourney.com/home>.
- [9] Joseph Redmon et al. “You only look once: Unified, real-time object detection”. In: *Proceedings of the IEEE conference on computer vision and pattern recognition*. 2016, pp. 779–788.
- [10] Nicolas Carion et al. “End-to-end object detection with transformers”. In: *European conference on computer vision*. Springer. 2020, pp. 213–229.
- [11] Matthias Minderer et al. “Simple open-vocabulary object detection”. In: *European conference on computer vision*. Springer. 2022, pp. 728–755.
- [12] Paul J Atzberger. “Importance of the mathematical foundations of machine learning methods for scientific and engineering applications”. In: *arXiv preprint arXiv:1808.02213* (2018).
- [13] Nathan Baker et al. *Workshop report on basic research needs for scientific machine learning: Core technologies for artificial intelligence*. Tech. rep. USDOE Office of Science (SC), Washington, DC (United States), 2019.
- [14] P J Atzberger B Quackenbush. “Geometric neural operators (gnps) for data-driven deep learning in non-euclidean settings.” In: *Machine Learning: Science and Technology* 5.4 (2024). ISSN: 2632-2153. DOI: <https://doi.org/10.1088/2632-2153/ad8980>. URL: <https://iopscience.iop.org/article/10.1088/2632-2153/ad8980>.
- [15] Panos Stinis, Constantinos Daskalakis, and Paul J Atzberger. “SDYN-GANs: Adversarial learning methods for multistep generative models for general order stochastic dynamics”. In: *Journal of Computational Physics* 519 (2024), p. 113442.
- [16] Nikola Kovachki et al. “Neural operator: learning maps between function spaces with applications to PDEs”. In: *J. Mach. Learn. Res.* 24 (2023), Paper No. [89], 97. ISSN: 1532-4435,1533-7928. DOI: [10.1080/15502287.2022.2066031](https://doi.org/10.1080/15502287.2022.2066031). URL: <https://doi.org/10.1080/15502287.2022.2066031>.

- [17] Tianping Chen and Hong Chen. “Universal approximation to nonlinear operators by neural networks with arbitrary activation functions and its application to dynamical systems”. In: *IEEE Transactions on Neural Networks* 6.4 (1995), pp. 911–917. DOI: [10.1109/72.392253](https://doi.org/10.1109/72.392253).
- [18] Filippo Bigi et al. “Fast evaluation of spherical harmonics with sphericart”. In: *J. Chem. Phys.* 159 (2023), p. 064802.
- [19] Xifeng Gao et al. “Robust structure simplification for hex re-meshing”. In: *ACM Trans. Graph.* 36.6 (Nov. 2017). ISSN: 0730-0301. DOI: [10.1145/3130800.3130848](https://doi.org/10.1145/3130800.3130848). URL: <https://doi.org/10.1145/3130800.3130848>.
- [20] Keenan Crane, Ulrich Pinkall, and Peter Schröder. “Robust fairing via conformal curvature flow”. In: *ACM Transactions on Graphics (TOG)* 32.4 (2013), pp. 1–10.
- [21] Ben J Gross et al. “Meshfree methods on manifolds for hydrodynamic flows on curved surfaces: A Generalized Moving Least-Squares (GMLS) approach”. In: *Journal of Computational Physics* 409 (2020), p. 109340. DOI: doi.org/10.1016/j.jcp.2020.109340. URL: <https://doi.org/10.1016/j.jcp.2020.109340>.
- [22] Nathan Bell et al. “PyAMG: Algebraic Multigrid Solvers in Python”. In: *Journal of Open Source Software* 8.87 (2023), p. 5495. DOI: [10.21105/joss.05495](https://doi.org/10.21105/joss.05495). URL: <https://doi.org/10.21105/joss.05495>.
- [23] C. Bane Sullivan and Alexander Kaszynski. “PyVista: 3D plotting and mesh analysis through a streamlined interface for the Visualization Toolkit (VTK)”. In: *Journal of Open Source Software* 4.37 (May 2019), p. 1450. DOI: [10.21105/joss.01450](https://doi.org/10.21105/joss.01450). URL: <https://doi.org/10.21105/joss.01450>.
- [24] Sebastien Valette, Jean-Marc Chassery, and Remy Prost. “Generic Remeshing of 3D Triangular Meshes with Metric-Dependent Discrete Voronoi Diagrams”. In: *IEEE Trans. Vis. Comput. Graph.* 14 (Mar. 2008), pp. 369–381. DOI: [10.1109/TVCG.2007.70430](https://doi.org/10.1109/TVCG.2007.70430).
- [25] Ben J Gross and Paul J Atzberger. “Hydrodynamic flows on curved surfaces: Spectral numerical methods for radial manifold shapes”. In: *Journal of Computational Physics* 371 (2018), pp. 663–689. DOI: doi.org/10.1016/j.jcp.2020.109340. URL: <https://doi.org/10.1016/j.jcp.2018.06.013>.
- [26] B Gross and Paul J Atzberger. “Spectral numerical exterior calculus methods for differential equations on radial manifolds”. In: *Journal of Scientific Computing* 76.1 (2018), pp. 145–165. DOI: doi.org/10.1007/s10915-017-0617-2. URL: <https://doi.org/10.1007/s10915-017-0617-2>.

A. Fundamental Forms, Curvature and Operators on Surfaces

We consider many geometric quantities that are computed from parameterizations of an surface. Using the parameterization $\boldsymbol{\sigma}(u, v)$ in variables (u, v) , the first fundamental form, \mathbf{I} , is defined as

$$\mathbf{I} = \begin{bmatrix} \boldsymbol{\sigma}_u \cdot \boldsymbol{\sigma}_u & \boldsymbol{\sigma}_u \cdot \boldsymbol{\sigma}_v \\ \boldsymbol{\sigma}_v \cdot \boldsymbol{\sigma}_u & \boldsymbol{\sigma}_v \cdot \boldsymbol{\sigma}_v \end{bmatrix} = \begin{bmatrix} E & F \\ F & G \end{bmatrix}. \quad (17)$$

This is also often referred to as the metric tensor, g , and is used for computations involving arc lengths and angles on the surface. The second fundamental form is defined as

$$\mathbf{II} = \begin{bmatrix} \boldsymbol{\sigma}_{uu} \cdot \mathbf{n} & \boldsymbol{\sigma}_{uv} \cdot \mathbf{n} \\ \boldsymbol{\sigma}_{uv} \cdot \mathbf{n} & \boldsymbol{\sigma}_{vv} \cdot \mathbf{n} \end{bmatrix} = \begin{bmatrix} L & M \\ M & N \end{bmatrix}, \quad (18)$$

where \mathbf{n} is the outward unit normal to the surface given by

$$\mathbf{n} = \frac{\boldsymbol{\sigma}_u \times \boldsymbol{\sigma}_v}{\|\boldsymbol{\sigma}_u \times \boldsymbol{\sigma}_v\|}. \quad (19)$$

The Weingarten map $\mathbf{W} = \mathbf{I}^{-1}\mathbf{II}$ is used to compute the the Gaussian curvature, K , and the mean curvature, H , of the surface. These are given by

$$K = \det(\mathbf{W}) = \frac{LN - M^2}{EG - F^2}, \quad (20)$$

$$H = \frac{1}{2}\text{tr}(\mathbf{W}) = \frac{1}{2} \left(\frac{LG - 2MF + NE}{EG - F^2} \right). \quad (21)$$

The Laplace-Beltrami operator, Δ_{LB} , is used to compute the Laplacian of a function on the surface. It is defined using the metric tensor and its inverse using Einstein notation as

$$\Delta_{LB} = \frac{1}{\sqrt{|g|}} \partial_i \left(g^{ij} \sqrt{|g|} \partial_j \right), \quad (22)$$

where $|g|$ denotes the determinant of the metric tensor and g^{ij} denotes the terms of the inverse metric.

B. Parameterizations of Surfaces and Data Generation

In this section we discuss parameterizations of surfaces used for data generation and training of the GNPs, namely radial and toroidal manifolds. For all shapes, once a parameterization is chosen, we generate a mesh and a quasi-uniform sampling of the surface using the PyACVD package from PyVista [23, 24]. The generated mesh is only used for sampling purposes.

A radial manifold is defined as a surface having the property that each point on the surface can be connected by a line segment to the origin only intersecting the surface at one point. This provides for a convenient parameterization \mathbf{x} of the surface in spherical coordinates as a function of the azimuth angle θ and the polar angle ϕ with

$$\mathbf{x}(\theta, \phi) = \boldsymbol{\sigma}(\theta, \phi) = r(\theta, \phi) \mathbf{r}(\theta, \phi). \quad (23)$$

The r is a positive scalar function and the \mathbf{r} is the unit vector from the origin to the point on the sphere with spherical coordinates (θ, ϕ) .

In practice, when performing coordinate-based calculations at least two charts are required for radial manifolds in order to overcome singularities that occur from the topology in the surface coordinate frames, such as poles when using spherical angles. To this end, when using our numerical methods we consider two coordinate charts as in [25, 26]. The first chart we call Chart A and has coordinate singularities at the north and south pole, while the latter chart we call Chart B which has coordinate singularities at the east and west poles, see [25, 26]. In practice, for a given $(\theta, \phi) \in [0, 2\pi) \times [0, \pi]$, we typically restrict usage of a chart for $\phi \in [\frac{\pi}{5}, \frac{4\pi}{5}]$. For chart A, we parameterize the manifold in the embedding space \mathbb{R}^3 as

$$\mathbf{x}(\hat{\theta}, \hat{\phi}) = r(\hat{\theta}, \hat{\phi})\mathbf{r}(\hat{\theta}, \hat{\phi}), \quad \mathbf{r}(\hat{\theta}, \hat{\phi}) = \left[\sin(\hat{\phi}) \cos(\hat{\theta}), \sin(\hat{\phi}) \sin(\hat{\theta}), \cos(\hat{\phi}) \right]. \quad (24)$$

For Chart B, we use

$$\mathbf{x}(\bar{\theta}, \bar{\phi}) = r(\bar{\theta}, \bar{\phi})\mathbf{r}(\bar{\theta}, \bar{\phi}), \quad \mathbf{r}(\bar{\theta}, \bar{\phi}) = \left[\cos(\bar{\phi}), \sin(\bar{\phi}) \sin(\bar{\theta}), \sin(\bar{\phi}) \cos(\bar{\theta}) \right]. \quad (25)$$

Using these parametrizations, we can compute the basis $\partial_\phi, \partial_\theta$ for the tangent space as

$$\boldsymbol{\sigma}_\phi(\theta, \phi) = r_\phi(\theta, \phi)\mathbf{r}(\theta, \phi) + r(\theta, \phi)\mathbf{r}_\phi(\theta, \phi), \quad (26)$$

$$\boldsymbol{\sigma}_\theta(\theta, \phi) = r_\theta(\theta, \phi)\mathbf{r}(\theta, \phi) + r(\theta, \phi)\mathbf{r}_\theta(\theta, \phi). \quad (27)$$

Expressions for $\mathbf{r}_\phi, \mathbf{r}_\theta$ can be found using equations 24 and 25 depending on which chart is being used. These can also be used to compute all the relevant quantities described in Appendix A.

We use radial manifolds in training and validation of the GNPs. We use spherical harmonics to generate radial functions $r(\theta, \phi)$ for the radial manifolds. In order to have a rich class of shapes for training, we consider a range of complexities for the radial functions. We sample complex coefficients a_l^m for $m = 0, \dots, l$ from a normal distribution with mean 0 and standard deviation $\frac{1}{l}$, to obtain the radial function

$$r(\theta, \phi) = \sum_{l=0}^L \sum_{m=-l}^l a_l^m Y_l^m(\theta, \phi), \quad (28)$$

where Y_l^m are the spherical harmonics. We choose a_l^m for $m < 0$ to ensure that $r(\theta, \phi)$ is real-valued. In order to have a range of complexities in the geometry, we truncate the series at $L = 3, 6, 8, 10, 12, 15, 18, 22$. Further, we translate and scale $r(\theta, \phi)$ so that it has mean 1 and satisfies $0.7 \leq r(\theta, \phi) \leq 1.3$ for all (θ, ϕ) .

For validation of the GNPs, we also consider toroidal manifolds. These are surfaces that are diffeomorphic to a torus. We consider the general parametrizations of

$$\boldsymbol{\sigma}(u, v) = ((a(u, v) \cos(v) + b(u, v)) \cos(u), (a(u, v) \cos(v) + b(u, v)) \sin(u), a(u, v) \sin(v)), \quad (29)$$

for $u, v \in [0, 2\pi)$. One can choose $a(u, v) = a, b(u, v) = b$ to obtain a standard torus. We consider functions $a(u, v), b(u, v)$ of the form

$$\begin{aligned} a(u, v) &= a_0 + r_0 \sin(A_0 u) \cos(B_0 v), \\ b(u, v) &= b_0 + r_1 \sin(A_1 u) \cos(B_1 v). \end{aligned} \quad (30)$$

We set $a_0 = \frac{1}{3}, b_0 = \frac{2}{3}$, and sample $r_0 \sim \mathcal{U}(0.05a_0, 0.2a_0), r_1 \sim \mathcal{U}(0, 0.08b_0)$. Further, we randomly select $A_i \in \{1, 2, \dots, 5\}$ and $B_i \in \{3, 4, \dots, 7\}$ to ensure a rich class of toroidal shapes. Using these parametrizations, we compute all relevant geometric quantities as described in [Appendix A](#) analytically using the Sympy package in Python and evaluate at each point on the surface.